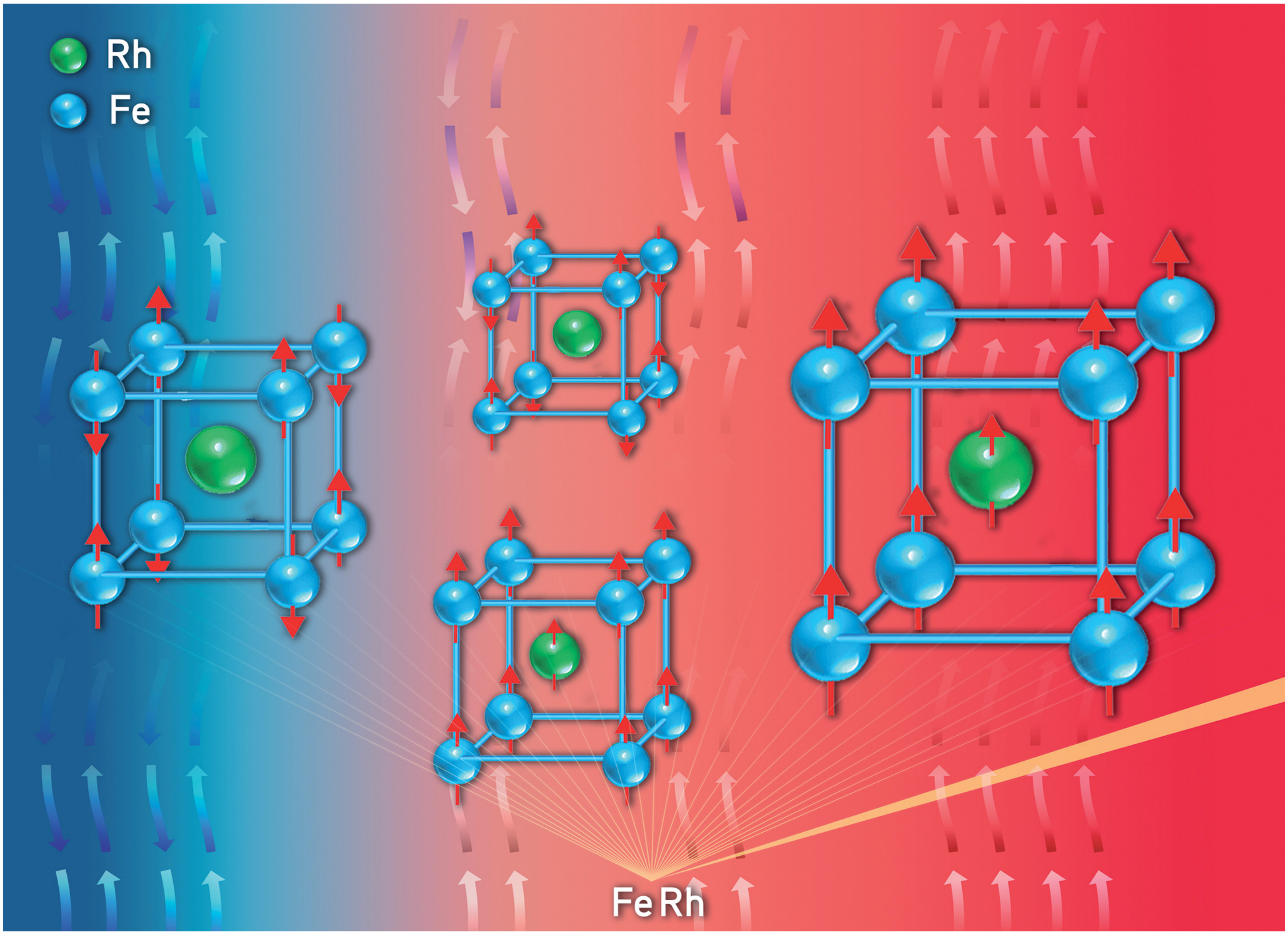

Research from Institut Laue-Langevin, ILL (France).

Scrutinizing the sharp magnetoelastic transition and kinetic arrest in $Fe_{49}Rh_{51}$ alloy using neutron thermo-diffraction

A kinetic arrest of the antiferromagnetic state in $Fe_{49}Rh_{51}$ alloy is evidenced by neutron thermo-diffraction experiments. Antiferromagnetic and ferromagnetic states coexist at least 70 K above the sharp magnetostructural transition.

Image reproduced by permission of Institut Laue-Langevin from *J. Mater. Chem. C*, 2025, **13**, 7017.

As featured in:

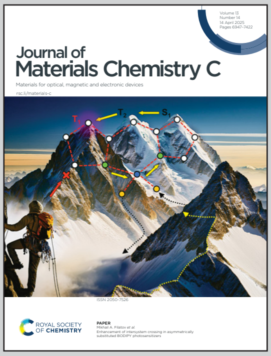
Volume 13
Number 14
14 April 2025
Pages 6947–7422

Journal of
Materials Chemistry C

Materials for optical, magnetic and electronic devices

rsc.li/materials-c

ISSN 2050-7526

ROYAL SOCIETY OF CHEMISTRY

PAPER
Mikhail A. Filatov *et al.*
Enhancement of intersystem crossing in asymmetrically substituted BODIPY photosensitizers

See J. L. Sánchez Llamazares, Pedro Gorria *et al.*, *J. Mater. Chem. C*, 2025, **13**, 7017.

ROYAL SOCIETY OF CHEMISTRY

rsc.li/materials-c

Registered charity number: 207890

Journal of
Materials Chemistry C

ROYAL SOCIETY
OF CHEMISTRY

PAPER

View Article Online
View Journal | View Issue

Check for updates

Cite this: *J. Mater. Chem. C*, 2025, **13**, 7017

Scrutinizing the sharp magnetoelastic transition and kinetic arrest in $Fe_{49}Rh_{51}$ alloy using neutron thermo-diffraction

K. Padrón-Alemán,[ab] G. J. Cuello,[a] I. Puente-Orench,[ac] J. Lopez-García,[bd] M. L. Arreguín-Hernández,[e] J. L. Sánchez Llamazares,*[f] Pedro Gorria*[bd] and P. Alvarez-Alonso[bd]

The $Fe_{49}Rh_{51}$ bulk alloy undergoes a sharp first-order magnetostructural transition from the antiferromagnetic (AFM) to ferromagnetic (FM) state around 332 K, accompanied by a drastic change of around 0.8% in the unit cell volume. Neutron thermo-diffraction experiments have been carried out to investigate the concomitant coupling between spin and lattice degrees of freedom in detail. Although it seems that the alloy entirely changes from the AFM to FM order in a very narrow temperature range (with a hysteresis of about 6 K), evidence of AFM order persists even 70 K above the first-order phase transition, suggesting a kinetic arrest of the AFM phase during both heating and cooling procedures. The estimated value for the Fe magnetic moment in the AFM phase at room temperature, around $\mu_{Fe} \approx 3.4\mu_B$, agrees with those already reported and reaches $3.8\mu_B$ at T = 10 K. However, in the FM phase, μ_{Fe} decreases to $\approx 2.3\mu_B$, while Rh acquires a magnetic moment of around $0.9\mu_B$. The use of temperature first-order reverse curves of neutron thermo-diffraction gives additional information about the magnetostructural coupling within the transition. Time-resolved neutron diffraction patterns collected at selected temperatures show that the alloy fully relaxes above the transition temperature, with both the magnetic and structural transformations occurring at the same temperature and with similar relaxation times.

Received 16th January 2025,
Accepted 25th February 2025

DOI: 10.1039/d5tc00193e

rsc.li/materials-c

Introduction

Binary $Fe_{100-x}Rh_x$ alloys with a near-equiatomic composition ($48 \leq x \leq 54$ at%) crystallize in the ordered CsCl-type crystal structure (also known as B2) and undergo a first-order magnetoelastic phase transition.[1,2] However, the intriguing mechanisms that govern the thermally- and magnetically-driven transformation, which is accompanied by a variation of approximately 1% of the unit cell volume, changing their magnetic structure from antiferromagnetic (AFM) to ferromagnetic (FM) (and *vice versa*),[1,2] remain unresolved.[1,3] Moreover, the characteristics of the phase transition strongly depend on the alloy fabrication methods, and the system is susceptible to minimal variations in composition.[4–7]

In addition, these alloys exhibit a giant magnetocaloric effect (GMCE) near room temperature (RT) associated with the spin–lattice coupling across the magnetoelastic transition.[1,8–12] Also, the structural transition in nearly equiatomic Fe–Rh alloys is sensitive to the applied mechanical stimuli such as stress and isostatic pressure, which leads to significant elastocaloric,[1,13] barocaloric,[14–16] and giant magnetostrictive effects.[17]

Recently, the investigation of the spin–lattice coupling looking for an answer to the question "what is the dominant factor driving the transition, the magnetic or the lattice structure?", has attracted much interest.[18–20] Nevertheless, contradictory information can be found, as most of the reported experimental studies have been carried out on thin films. Hence, there needs to be more information regarding the behaviour of bulk alloys.[20,21] Aiming to fill this gap, precise knowledge of the evolution of the magnetic moments for Fe and Rh atoms, together with the unit cell volume through the phase transition, is mandatory to characterize the magneto-structural transformation. Magnetic moments at the Fe sites of around $3.3\mu_B$ in the AFM region have been estimated through neutron scattering and Mössbauer spectroscopy experiments,[22–25] and *ab initio*

---

[a] *Diffraction Group, Institut Laue-Langevin, 71 Ave des Martyrs, CS 20156, 38042 Grenoble cedex 9, France*

[b] *Departamento de Física, Universidad de Oviedo, Calvo Sotelo 18, 33007 Oviedo, Spain. E-mail: pgorria@uniovi.es*

[c] *Instituto de Nanociencia y Materiales de Aragón (INMA-CSIC), C/Pedro Cerbuna, 12, 50009 Zaragoza, Spain*

[d] *Instituto Universitario de Tecnología Industrial de Asturias, Universidad de Oviedo, Gijón 33203, Spain*

[e] *Centro de Nanociencias y Nanotecnología, Universidad Nacional Autónoma de, MéxicoAP 14, Ensenada 22860, Baja California, Mexico*

[f] *Instituto Potosino de Investigación Científica y Tecnológica A. C., Camino a la presa San José 2055, 78216, San Luis Potosí, Mexico. E-mail: jose.sanchez@ipicyt.edu.mx*

calculations.[26–28] Rh atoms have negligible magnetic moments in the AFM phase,[22,27,29] whereas it is well documented that their magnetic moment is $\sim 0.9\mu_B$ when these alloys are in the pure FM region.[22,23,27,30] Different values for the magnetic moment of the Fe atoms in the FM phase have been reported, from $3.2\mu_B$ (close to the value in the AFM region,[22,23,30,31]) to $2.84\mu_B$,[24] $2.5\mu_B$,[32] $2.2\mu_B$,[33,34] and $2.85\mu_B$.[35] These differences may arise from the experimental techniques used for the estimation of the magnetic moment value, as well as the specific chemical composition of the alloy or the preparation procedure, such as the thermal annealing conditions (temperature and time) and/or the cooling process of the alloy from the selected annealing temperature. It is worth noting that there is no detailed information regarding the temperature evolution of the magnetic moments of Fe and Rh atoms in the Fe–Rh system in either AFM or FM regions.

On the other hand, the values reported for the cell parameter vary from 2.97 Å to 3.00 Å,[4,36,37] and its temperature dependence is again affected by the fabrication method and/or the alloy composition.[4,32] Although a direct connection between the temperature evolution of the cell parameter and that of the magnetic moment has not been reported, a rapid drop of the intensity of the AFM peak $(\frac{1}{2}\frac{1}{2}\frac{1}{2})$ together with a sharp increase in lattice parameter has been observed in neutron diffraction (ND) patterns at the same temperature.[21] Also, a clear correlation has been observed between the temperature dependences of the lattice parameter and the magnetic moment estimated from X-ray magnetic circular dichroism measured at the Fe K and Rh L2 edges, around the structural transformation temperature within an uncertainty of ±2 K.[19] Using femtosecond optical pulses to analyse this magneto-structural coupling suggests that the spin orientation across the AFM to FM transition occurs faster than the lattice expansion (in several ps).[38] Thus, the spin subsystem drives the transformation, which is accompanied by lattice expansion.[38,39] However, some authors have reported that the AFM to FM transition has two timescales, one where the initial nucleation of the FM nuclei occurs with the same timescale for the magnetic and structural development, and the second for the growth and alignment of the ferromagnetic nuclei along the applied magnetic field.[20,40]

In this work, we investigate the dynamics and the spin–lattice coupling of the phase transition in a bulk induction melted $Fe_{49}Rh_{51}$ alloy by using neutron thermo-diffraction and analysing the temperature evolution of the nuclear and magnetic structures. This technique allows us to characterize and compare both transformations simultaneously in the same experiment, which avoids uncertainty in the values of the temperatures when results from different experimental techniques are compared. To fulfil this goal, neutron thermodiffraction patterns were collected to determine the temperature dependence of the phase fractions, magnetic moments, and the lattice parameter. In addition, time-resolved neutron diffraction patterns were collected to investigate the dynamic evolution of the magnetic and nuclear structure during relaxation and to obtain insight into the spin–lattice coupling. Besides this, we obtained temperature first order reverse curves of neutron diffraction, *T*-FORC (ND), to examine how the magnetic and nuclear structures evolve in the area enclosed by the thermal hysteresis region.

Experimental details

The binary $Fe_{49}Rh_{51}$ alloy was fabricated by induction melting from high-purity iron and rhodium elements. The induction-melted alloy was subsequently processed to ensure phase homogenization through thermal annealing at 1000 °C for 48 hours followed by iced water quenching. Details of the preparation can be found elsewhere.[7]

Neutron diffraction experiments were carried out at the Institut Laue–Langevin (ILL) in Grenoble, France. Neutron thermo-diffraction patterns were collected in the two-axis D1B powder diffractometer in the 0.0–4.5 ($Å^{-1}$) Q-range, using a wavelength of $\lambda = 2.52$ Å. The neutron diffraction patterns were collected every 2 min in the temperature range from 100 to 485 K on heating and from 485 to 10 K on cooling using a cryofurnace. Two different temperature ramps were used: (i) 0.25 K min^{-1} in the FOPT region, and (ii) 1.0 K min^{-1} outside this region. The full profile fitting of the ND patterns was done using the FullProf suite package,[41,42] based on the Rietveld method,[43] with reasonably good reliability factors.

Time-resolved neutron diffraction patterns were measured in the D20 instrument, a high-flux two-axis diffractometer, using a cryofurnace. A take-off angle of 42° and $\lambda = 2.41$ Å were used in the experimental configuration. A set of temperatures (330, 332, and 333 K) on the edge and inside the FOPT region were selected for this experiment. The samples was heated up to each of these selected temperatures starting at a temperature at which the material is in AFM state (300 K). Neutron diffraction patterns were acquired every 12 s on heating the sample with a temperature sweep rate of 0.5 K min^{-1}. Once the relaxation temperature (T_{Relax}) was reached and stabilized (this time chosen as $t = 0$ s), neutron diffraction patterns were measured every 12 s for a time interval of 10 min. After that, the sample was cooled down to 300 K to start the same procedure for the next T_{Relax}.

Magnetization measurements were performed using a vibrating sample magnetometer (VSM) option of a quantum design PPMS® Dynacool®-9T system. The temperature dependence of magnetization, $M(T)$ curves, under a low applied magnetic field ($\mu_0 H = 5$ mT) was measured on heating and on cooling in a temperature range covering the AFM–FM and FM–AFM transitions (270 K ↔ 360 K). Isothermal magnetization curves, $M(H)$, were measured between 0 and 3 T for selected temperatures after the first-order phase transition ($T = 340$, 350, 360, 370, 380, 400, 450, and 500 K). We estimated the magnetic moment per formula unit by fitting the high-field region of the $M(H)$ curves to an approach-to-saturation law.[44] Then, we compared these results with the values obtained from the fit of the magnetic structure of neutron diffraction patterns.

T-FORC analysis

First-order-reversal-curve (FORC) analysis was originally developed to investigate magnetic interactions and coercivity distributions in magnetic materials exhibiting hysteresis in the magnetization *versus* applied magnetic field curves.[45] This type of analysis has recently been extended to gain insight into the first-order phase transitions that some magnetocaloric materials display with a significant thermal hysteresis but changing the applied magnetic field by the temperature as an external stimulus. Therefore, the temperature-first-order-reversal-curve (T-FORC) distribution represents a novel method for investigating the magnetic interactions within the $M(T)$ curves around the first-order phase transitions.[46] T-FORC provides a tool for revealing hidden interactions within the minor cycles of a magnetization *versus* temperature hysteresis loop, enabling the fingerprinting of phase transitions and facilitating comparisons across different materials.[46–48]

The T-FORC distributions were determined from the $M(T)$ curves measured inside the thermal hysteresis loop by calculating the second derivative of the magnetization with respect to the temperature and the reverse temperatures (see eqn (1)).[46] Plus and minus signs are chosen for the calculation of the distribution of the FM → AFM and AFM → FM transition, respectively.

$$\rho_{\mathrm{M}}(T,\ T_{\mathrm{R}}) = \pm\frac{\partial^2 M(T, T_{\mathrm{R}})}{\partial T_{\mathrm{R}}\partial T} \tag{1}$$

In this work, we propose to extend this analysis to the thermal hysteresis exhibited by the lattice parameter (a) and the fraction of the AFM phase (f_{AFM}) of a $\mathrm{Fe_{49}Rh_{51}}$ sample to fingerprint both the magnetic and structural transformations. To fulfill this purpose, a series of neutron diffraction patterns were collected during heating/cooling procedures within the temperature range of the magnetoelastic transition. In the following, we will use T-FORC(M) for the conventional T-FORC method based on analyzing the $M(T)$ curves to avoid misinterpretations. In this way, we propose T-FORC(NDa) and T-FORC(NDf_{AFM}) for the lattice parameter and the fraction of the AFM phase, respectively, obtained from neutron thermo-diffraction patterns. Hence, the T-FORC corresponding to the distribution of the lattice parameter values is defined as:

$$\rho_{\mathrm{a}}(T, T_{\mathrm{R}}) = \pm\frac{\partial^2 a(T,T_{\mathrm{R}})}{\partial T_{\mathrm{R}}\partial T} \tag{2}$$

and that for the fraction of the AFM phase:

$$\rho_{f_{\mathrm{AFM}}}(T,\ T_{\mathrm{R}}) = \pm\frac{\partial^2 f(T, T_{\mathrm{R}})}{\partial T_{\mathrm{R}}\partial T} \tag{3}$$

To calculate the T-FORC(NDa) and T-FORC(NDf_{AFM}) distributions for the FM–AFM transition, it is necessary to define a temperature at which the material is entirely in the AFM state, called the saturation temperature, T_{S} = 300 K. Additionally, a set of temperatures along the heating branch of the transformation and in the region of the transition, called reverse temperatures T_{R}, must be selected. To obtain the reverse or T-FORC curve, the temperature must be increased from T_{S} to a reverse temperature T_{Ri} (step 1 → 2) and then decreased down to T_{S} (step 2 → 1), measuring the corresponding neutron diffraction patterns. These steps are repeated for each T_{Ri}. The values of both a and f_{AFM} are obtained from the Rietveld refinement of each neutron diffraction pattern collected between T_{Ri} and T_{S}. Then, the T-FORC(NDa) and T-FORC(NDf_{AFM}) distributions are calculated using eqn (2) and (3), respectively. This method gives us detailed and complementary information on spin–lattice coupling, providing insight into the dynamics of the structural and magnetic phase transition, thus offering a deeper understanding of the magnetoelastic behavior.

In addition, we also show the temperature first order reverse curve of magnetization T-FORC(M) measured under a low magnetic field (5 mT) for the FM–AFM phase transformation. The followed protocol is very similar to the one previously explained for T-FORC(ND). In this case, T_{S} = 270 K, the distribution was calculated using eqn (1), and the magnetic field was fixed to 5 mT during the 1 → 2 and 2 → 1 steps of the protocol.

Results and discussion

Neutron thermo-diffraction

Fig. 1(a) and (b) show the neutron diffraction patterns in the AFM phase (10 K) and in the FM phase (480 K), respectively, measured in the D1B instrument, together with the Rietveld refinement.[41,42]

The intensity peaks coming from the nuclear contribution can be indexed as the Bragg reflections corresponding to the CsCl B2-type crystal structure (space group $Pm\bar{3}m$). The Fe and Rh atoms are located at (0, 0, 0) and (0.5, 0.5, 0.5) positions of the unit cell, respectively (see the insets in Fig. 1). The magnetic structure at low temperatures coincides with the AFM-II type as reported before,[1] and changes to FM at high temperature with the expected co-lineal alignment of the Fe and Rh magnetic moments.[1] The refinement of the magnetic structure at 10 K gives a value of $(3.8 \pm 0.1)\mu_{\mathrm{B}}$ for the magnetic moment of the Fe atom, higher than those previously reported.[22,24] In contrast, Rh atoms do not carry any magnetic moment in agreement with previous works.[1] In the FM region, small changes in the Rh magnetic moment may not significantly affect the Rietveld refinement of the magnetic structure, so, it was kept fixed to $0.9\mu_{\mathrm{B}}$.[32] Otherwise, the fit does not converge or give rise to non-physical values.[32] On the other hand, the calculated magnetic moment of Fe in the FM phase is considerably lower than that in the AFM one, $\mu_{\mathrm{Fe\text{-}FM}} = (2.2 \pm 0.2)\mu_{\mathrm{B}}$, at T = 480 K, in good agreement with other published values,[33–35] and with the values we have estimated from the isothermal magnetization curves (see below).

In Fig. 2 the evolution of selected regions of the ND patterns, where the most intense nuclear (110) and AFM peaks appear, during heating (left panel) and cooling (right panel) procedures can be visualized. The contour maps in Fig. 2(a) and (b) clearly show the occurrence of the FOPT; see, for instance, the abrupt shift of the (110) peak to lower Q values (increase in the lattice parameter) at high temperature. On heating, the AFM–FM phase transition starts around 332 K, and finishes approximately at 338 K, while on cooling, the reverse transformation (FM–AFM) occurs between 330 and 324 K.

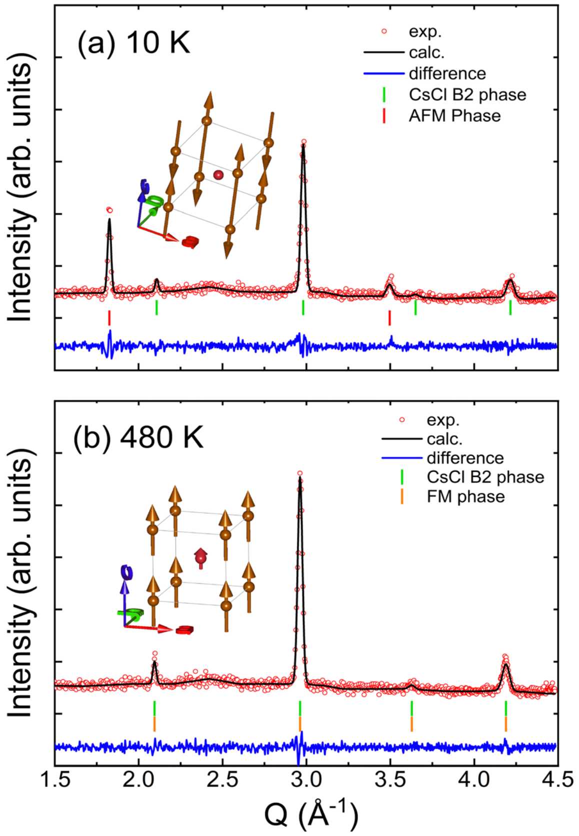

Fig. 1 Neutron diffraction patterns collected at (a) 10 K (AFM) and (b) 480 K (FM) together with the Rietveld fits. The insets illustrate schematically the magnetic and nuclear structures in both magnetically ordered states.

In Fig. 2(c) and (d) a particular region of the ND patterns collected at 6 selected temperatures are depicted. The peak located at $Q \approx 2.96$ Å^{-1} corresponds to the (110) Bragg reflection of the nuclear structure, and that at $Q \approx 1.826$ Å^{-1} (see the vertical arrow) is purely magnetic and comes from the AFM phase. The variation of the intensity of the AFM peak with temperature is better observed in the contour maps in Fig. 2(e) and (f). It is worth noting that a meticulous analysis suggests the presence of the AFM peak almost 70 K above the temperature for the FOPT during heating. This unreported feature is also observed when cooling from high temperatures; the AFM peak starts to appear at around the same temperature ($T \approx 400$ K). Even though the alloy exhibits FOPT within a narrow temperature interval ($\approx$6 K), a small AFM phase volume fraction remains stable, coexisting with the predominant FM phase for at least 70 K above the transformation. This phase coexistence behavior, known as the kinetic arrest of the magnetostructural transition, was previously observed only in FeRh thin layers.[18] Recently, a somewhat "opposite" phenomenon has been reported in another off-stoichiometric FeRh alloy with a slight excess of Fe ($Fe_{51}Rh_{49}$), in which residual FM regions (a minor portion of the sample, around 10%) subsist even below the FM–AFM transition down to 5 K.[49]

The mechanism for the kinetic arrest can be explained as follows: on heating the alloy, once the magnetostructural transition starts, the FM phase grows at a fast rate until the sharp change of the lattice parameter is completed. After that, the remaining AFM phase transforms progressively into the FM one. Asymmetrically, on cooling from a high temperature, the AFM phase starts to grow slowly at around 400 K, and when the temperature for the FOPT is reached, the system fully transforms into the AFM state. Therefore, two distinct processes seem to drive the phase transformation: (i) a sharp first-order-like AFM-to-FM/FM-to-AFM transition concurring with the sharp variation of the cell parameter (FOPT region); and (ii) a smooth second-order-like transition in the temperature range of the kinetic arrest for the AFM phase.

In order to achieve precise information about the evolution of the magnetic moment of both Fe and Rh across the FOPT on heating and cooling, we have analyzed the ND patterns collected in a wide temperature range taking into account three different regions for the fit of the patterns: (i) the region in which only the AFM phase is present (below 330 K); (ii) the region in which only the FM phase is present (above 400 K); and (iii) the region in which both phases coexist. Fig. 3 shows the results of such analysis. The temperature dependence of the Fe magnetic moment on heating from low temperature and on cooling from high temperature is depicted in Fig. 3(a) and (b), respectively.

The drastic change in the value of μ_{Fe} across the magnetostructural transition is observed and is closely connected to the features discussed in the previous paragraph. The magnetic moment of Fe in the AFM phase reaches a value of $\mu_{\mathrm{Fe}} \approx (3.8 \pm 0.1)\mu_{\mathrm{B}}$ at $T = 10$ K and decreases slowly to $(3.4 \pm 0.1)\mu_{\mathrm{B}}$ at RT. The trend of μ_{Fe} *vs.* T is similar in heating and cooling procedures (see Fig. 3 left panel). In the pure FM region, the value for the Fe magnetic moment is significantly smaller. It decreases progressively as the temperature is raised, as expected, from about $(2.3 \pm 0.2)\mu_{\mathrm{B}}$ to $(2.0 \pm 0.2)\mu_{\mathrm{B}}$ at $T = 500$ K.

In the right panel of Fig. 3, we show the temperature evolution of the total magnetic moment per formula unit, estimated from the fit of the high field region of the $M(H)$ curves to an approach-to-saturation law [Fig. 3(c)]; and from the fit of the ND patterns [see Fig. 3(d) and (e)]. It is worth noting that the temperature evolution of the magnetic moment per formula unit, μ_{B} f.u.$^{-1}$, looks relatively smooth in the three graphs. The reason for that is the appearance of magnetic moment in Rh atoms in the FM phase ($\mu_{\mathrm{Rh}} \approx 0.9 \pm 0.1)\mu_{\mathrm{B}}$, that align parallel to those of Fe atoms, compensating the reduction of μ_{Fe} from the AFM to FM state, and thus giving rise to a similar value (above $3\mu_{\mathrm{B}}$) for the total magnetic moment.

However, the neutron diffraction patterns do not possess enough resolution to discriminate the nuclear peaks from the AFM and FM phases within the coexistence region (the difference in cell volume is of around 1%). Therefore, the AFM magnetic phase was scaled together with the FM nuclear and magnetic phases within the coexistence region for the Rietveld refinement of the ND patterns. Due to this constraint, the magnetic moment of AFM Fe ($\mu_{\mathrm{Fe\text{-}AFM}}$) cannot be precisely determined in this temperature range and was kept constant at a value of $3.4\mu_{\mathrm{B}}$ (the value just before the FOPT transition starts). The latter allows

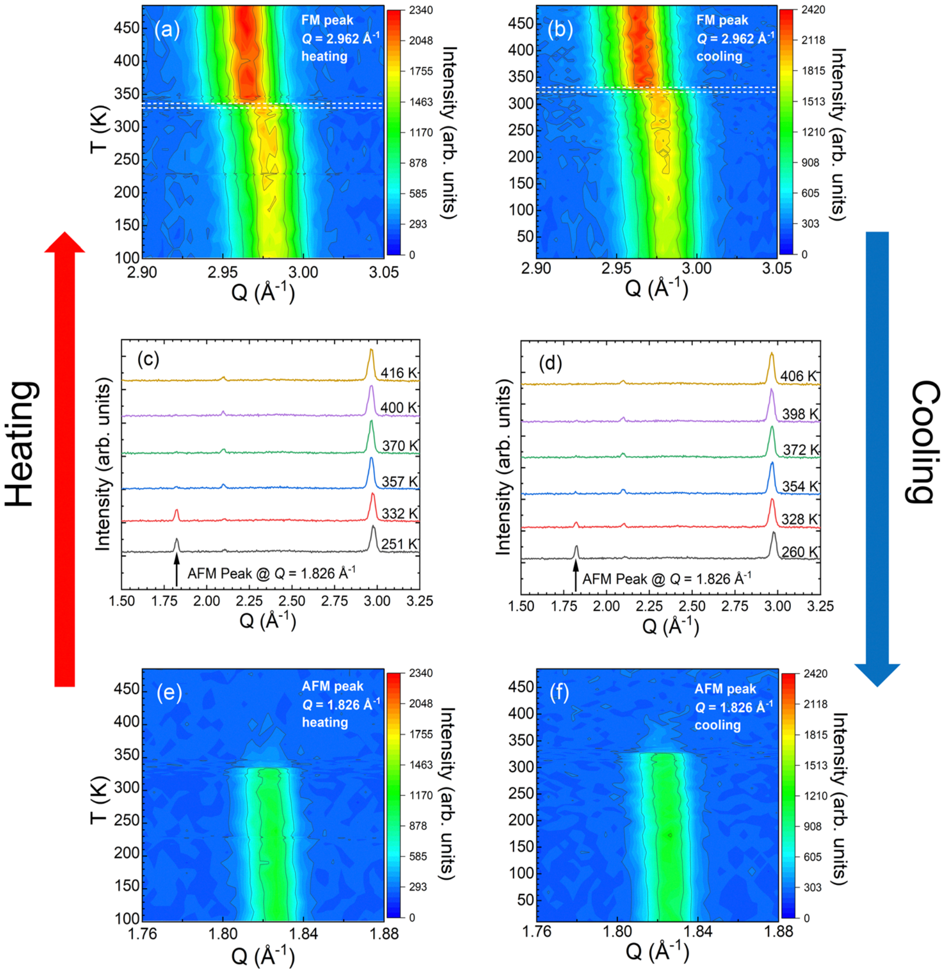

Fig. 2 Contour map of the high-intensity FM/nuclear peak of the neutron diffraction patterns (a) on heating from 100 to 485 K and (b) on cooling from 485 to 10 K. Evolution of the high-intensity AFM peak with temperature, (c) heating and (d) cooling. Contour map of the high-intensity AFM peak of the neutron diffraction patterns (e) on heating from 100 to 485 K, and (f) on cooling from 485 to 10 K. The white horizontal dashed lines in (a) and (b) show the first-order AFM–FM and FM–AFM phase transition ranges, respectively.

us to get approximate values of the AFM phase fraction f_{AFM} as a function of temperature (see below).

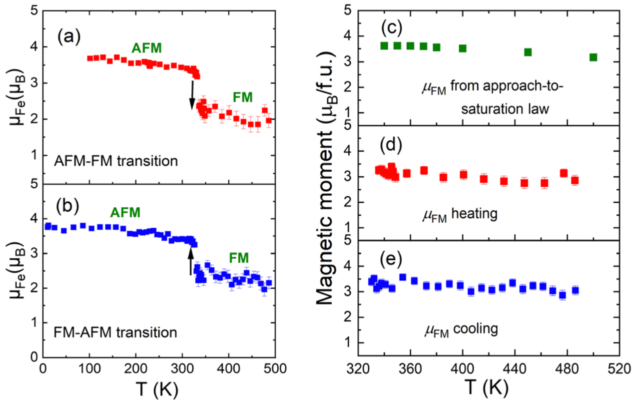

Fig. 3 Temperature evolution of the magnetic moment of Fe atoms (a) on heating, and (b) on cooling. Temperature evolution of the magnetic moment per formula unit estimated from: (c) $M(H)$ curves; (d) and (e) from neutron diffraction patterns. The arrows in (a) and (b) illustrate the change of Fe magnetic moment between the AFM and FM phases.

The abrupt change in the lattice parameter around $T = 330$ K on heating/cooling procedures is a signature of a FOPT [see Fig. 4(a), for a selected temperature range near the FOPT and the inset for the entire temperature range of the measurements], that exhibits a thermal hysteretic behavior between heating and cooling processes. In Fig. 4(b), we plot the temperature evolution of the AFM phase fraction, $f_{AFM}(T)$ obtained from the fit of the ND patterns as mentioned above [see the inset for that of the FM phase fraction, $f_{FM}(T)$]. Both curves are flat for temperatures below those of the FOPT, indicating that all the sample is in an AFM state. However, this is not the case for the curves above the FOPT. These $f_{AFM}(T)$ curves show a negative and small slope, suggesting that the whole sample has not fully transformed into the FM state, thus evidencing a kinetic arrest of the AFM phase. A similar trend is observed in the $f_{FM}(T)$ curves with a small and positive slope above the FOPT. In fact, the unit cell volume expansion is $\approx$0.8% across the FOPT and reaches 1% only around $T = 400$ K, where the kinetically arrested AFM phase fraction is almost zero. The latter reveals that even after the completion of the FOPT in a 6 K-interval, approximately 20% of the AFM phase

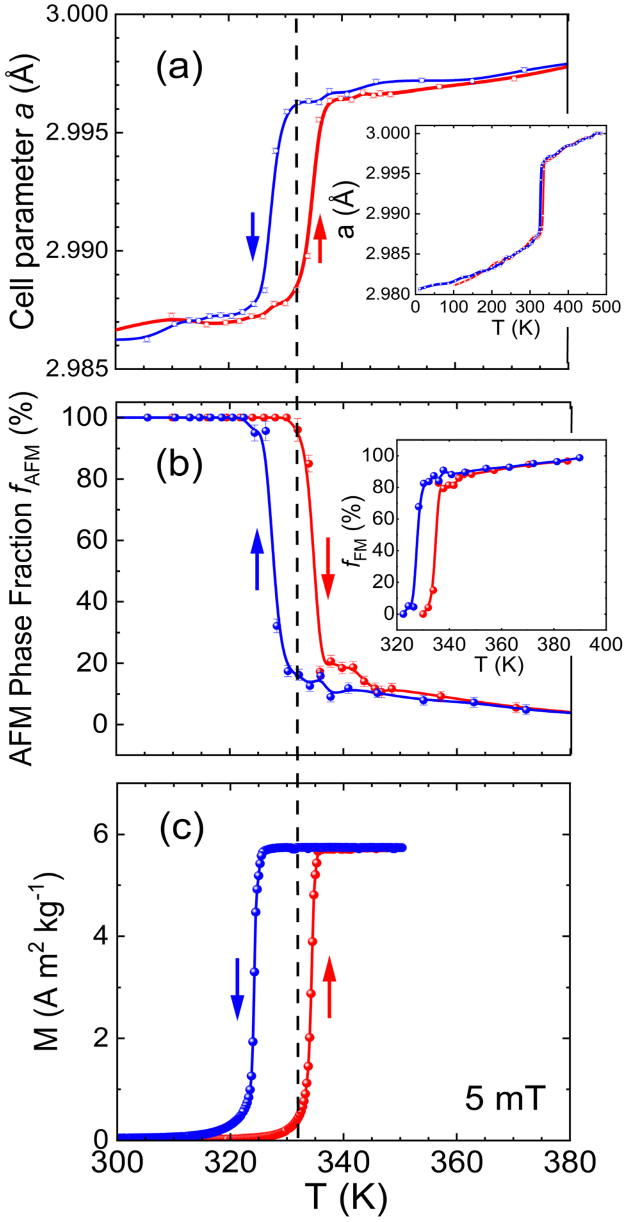

Fig. 4 Temperature dependence of (a) the cell parameter *a*, (b) the AFM phase fraction (inset depicts that of the FM phase fraction), and (c) the magnetization under a magnetic field of 5 mT. The vertical dashed line highlights the transition temperature (T_t) coincidence for the three curves during the heating process.

remains arrested, as also observed in the neutron diffraction maps (see Fig. 2). This residual AFM fraction decreases as the temperature rises, following a transformation pattern resembling a second-order phase transition, as mentioned above.

If we observe the magnetization *versus* temperature curve under an applied magnetic field of 5 mT [see Fig. 4(c)], it is clear that the three magnitudes, the lattice parameter, the fraction of the AFM phase, and the magnetization, follow a similar behavior across the FOPT (see Fig. 4).

In Table 1, the characteristic temperatures involved in the FOPT and obtained from data in Fig. 4 are gathered, together with the maximum of the temperature derivative of $a(T)$, $f_{AFM}(T)$, and $M(T)$ curves. We must mention that the obtained value for the $\Delta T_{hyst} = [AF_s + AF_f - (FA_s - FA_f)]/2$ associated with the hysteresis is slightly higher for the $M(T)$ curve, probably due to the different heating and cooling rates in both neutron thermo-diffraction and magnetization experiments.

T-FORC of neutron diffraction

To compare the evolution of the structural and magnetic phase transitions within the area enclosed by the thermal hysteresis loop [see Fig. 4(a) and (b)], *T*-FORC(ND*a*) for the lattice parameter and *T*-FORC(NDf_{AFM}) for the fraction of the AFM phase distributions were calculated. We obtain the $a(T)$ and $f_{AFM}(T)$ recoil curves from the Rietveld refinement of the ND patterns recorded from the reverse temperature T_{Ri} to T_S = 300 K. A locally weighted scatterplot smoothing method has been used to decrease the noise of the data [see Fig. 5(a) and (c)].

Fig. 5(b) and (d) show the *T*-FORC(ND*a*) and *T*-FORC(NDf_{AFM}) distributions, with zero values at temperatures below T_R = 332 K, corresponding to the *T* region before the FOPT on heating. In the temperature region of phase coexistence, the distributions gain positive values, reaching their maxima at 328 K. At higher T_R, the positive area of the distribution is reduced, but leaving a positive tail [not so well-defined in the *T*-FORC(NDf_{AFM})] until the end of the diagram at T_R = 337 K. This might be associated with the kinetic arrest of the AFM phase and its interaction with the FM phase in this *T* interval region. Both *a* and $f_{AFM}(T)$ diagrams closely share the same shape and features. The differences could be associated with data treatment procedures. Since these distributions are derived from the derivatives (see eqn (1) and (2)), we can assume that both transitions evolve similarly due to the changes introduced during the phase transformation process. Moreover, they follow the same dynamics to complete the phase transformation for each reverse curve, conserving the hand-in-hand evolution of the magnetic and structural transformation within the hysteresis area. This finding underscores the interdependent evolution of spin and lattice structures throughout the transition.

Table 1 Initial (AF_S, FA_S) and final (AF_f, FA_f) temperatures of the magnetoelastic transition, thermal hysteresis (ΔT_{hyst}), and temperature at which the temperature derivatives d*M*/d*T*, d*a*/d*T*, and $|df_{AFM}/dT|$ reach their maximum values

						$\lvert d(M, a, f_{AFM})/dT(T)\rvert^{max}$ (K)	
Quantity	AF_s (K)	AF_f (K)	FA_s (K)	FA_f (K)	ΔT_{hyst} (K)	AFM → FM	FM → AFM
$M(T)^{5\ mT}$	332	334	324	322	10	333	323
$a(T)$	332	338	330	324	8	334	328
$f_{AFM}(T)$	332	338	330	324	8	334	328

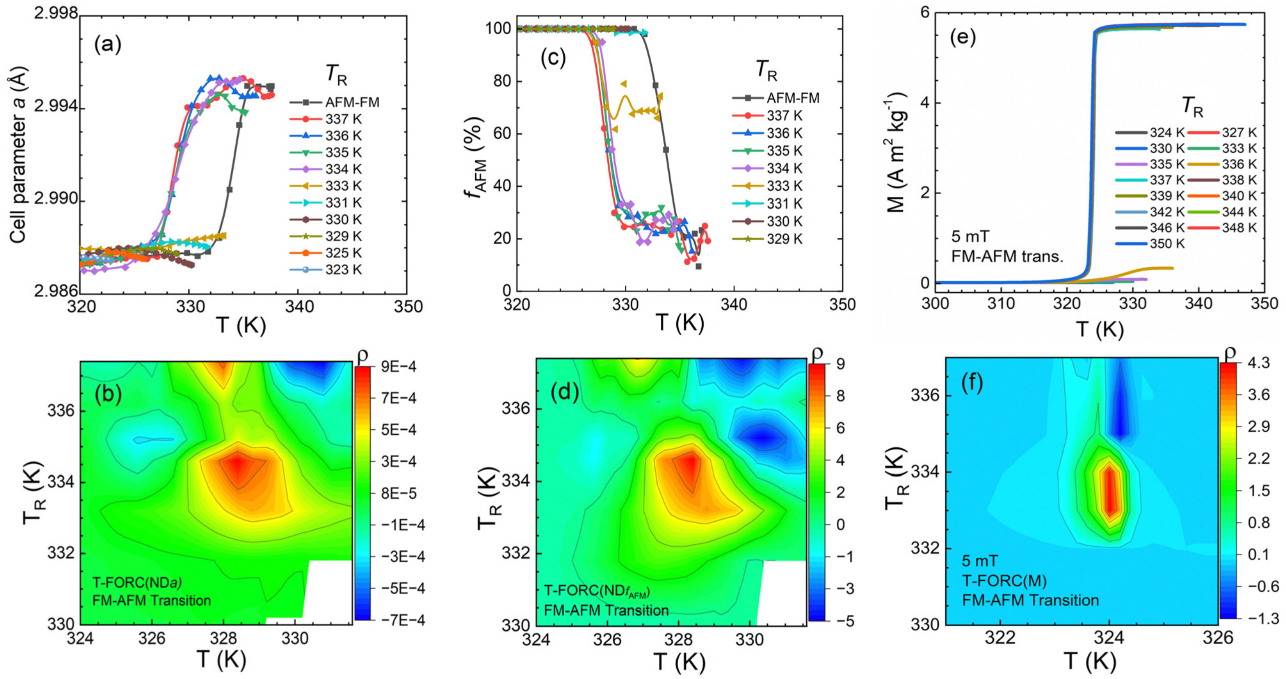

Fig. 5 (a) Reverse temperature and (b) *T*-FORC distribution linked to the FM → AFM transition in terms of the temperature evolution of the lattice parameter *a*. (c) Reverse temperature and (d) *T*-FORC distribution associated with the evolution of the magnetic phase transformation of the AFM state in the FM → AFM transition. (e) Reverse temperature and (f) *T*-FORC diagram for the magnetization under a magnetic field of 5 mT in the FM → AFM transition.

Fig. 5(e) and (f) show the reverse curves from the thermomagnetic measurements under $\mu_0 H$ = 5 mT for each T_{Ri}, and the corresponding *T*-FORC magnetization distribution, respectively. *T*-FORC(*M*) offers higher statistical reliability, eliminating the need for smoothing and resulting in a better-quality diagram. Four main regions can be identified: the maximum of the distribution, the positive area surrounding the maximum, and the positive and negative tails extending toward higher T_R values. Although the center and width of the *T*-FORC(*M*) diagram differ from *T*-FORC(ND*a*) and *T*-FORC(ND*f*) due to the applied magnetic field that slightly affects the transformation temperatures, the four areas highlighted above are observed on the *T*-FORC distributions obtained from neutron thermo-diffraction measurements. Hence, we assume that the *T*-FORC(ND*a*) and *T*-FORC(NDf_{AFM}) accurately describe the phase transformation. Hence, experimental artifacts derived from structural refinement or smoothing treatments can be discarded. Indeed, the negative tail in the distributions, at the right and before the FOPT, of the main spot of *T*-FORC(ND*a*) and *T*-FORC(NDf_{AFM}) could be interpreted as noise, but this negative part also appears in the best-defined *T*-FORC(*M*) distribution, suggesting that it is a feature connected to the phase transformation. The variation among the reverse curves of two possible different transformation rates in the edge and after the phase transition could be responsible for this finding. Then, a complete explanation of this observation could be the subject of further study.

Time-resolved neutron diffraction

Fig. 6(a) and (b) show the time evolution of the cell parameter and the fraction of the AFM phase at three characteristic temperatures: (i) T_{relax} = 330 K < T_T; (ii) T_{relax} = T_T = 332 K; and (iii) T_{relax} = 333 K > T_T. The inset in Fig. 6(d) illustrates the values of the cell parameter and the fraction of the AFM phase corresponding to each T_{relax} along the overall $a(T)$ and $f_{AFM}(T)$ curves. Starting at T = 300 K (AFM phase), the sample is heated up to T_{relax}, and keeping it constant, several ND patterns are collected every 12 seconds. The negative time in Fig. 6(a) and (b) represents the time while heating the sample from T = 300 K to T_{relax}. At T_{relax} = 330 K we do not observe variation of a and f_{AFM} during the measured time [red points in Fig. 6(a) and (b)], indicating the absence of relaxation in any of the two structures.

Repeating the same procedure for T_{relax} = T_T = 332 K, after t = 0 s a small increment in both a and f_{AFM} is depicted [see the blue points in Fig. 6(a) and (b)], indicating a relaxation of the alloy into the FM phase: a small portion of the sample (less than 10%, considering the error bars) changes from the AFM to FM state. However, for T_{relax} = 333 K [green points in Fig. 6(a) and (b)], the sample, which contains approximately 85% of the AFM phase a t = 0 s relaxes and fully completes the AFM → FM magnetoelastic transition within approximately 120 seconds. The relaxation time for T_{Relax} = 333 K was calculated from the fit of eqn (4) and (5), analogous to the equation $\frac{M}{M_S} = 1 - B \times e^{-\frac{t}{\tau}}$ that describes a viscous magnetic system,[50,51] to the relaxation curves [see Fig. 6(c) and (d)].

$$\frac{a}{a_S} = 1 - \mathrm{B} \times e^{-\frac{t}{\tau}} \tag{4}$$

$$\frac{f_{AFM}}{f_{S\text{-}AFM}} = 1 + B \times e^{\frac{t}{\tau}} \tag{5}$$

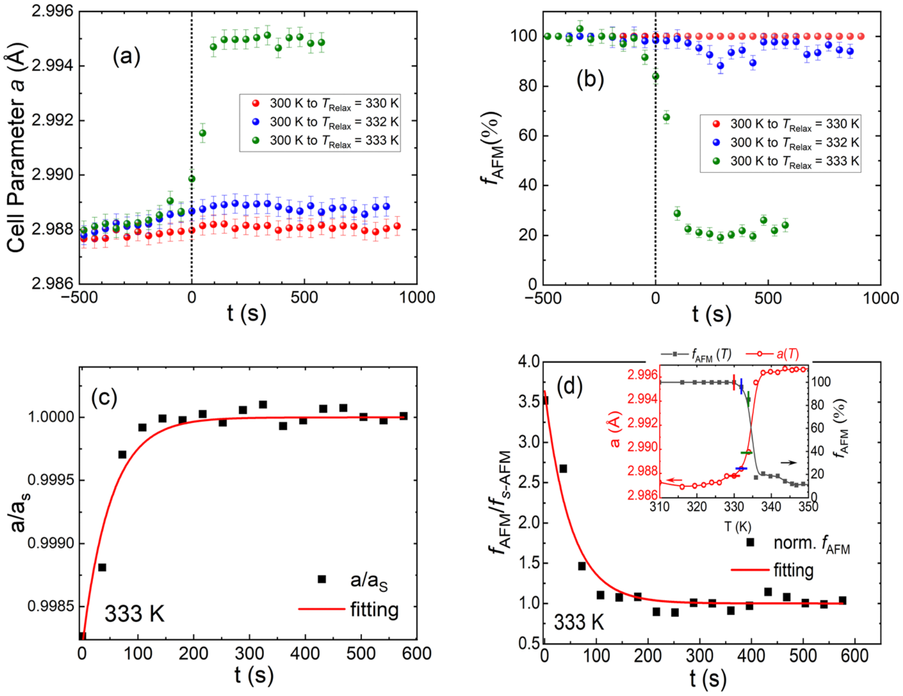

Fig. 6 Time evolution of the (a) lattice parameter, a, and (b) AFM fraction, f_{AFM}, at T_{relax} = 330 K (red points), 332 K (blue points), and 333 K (green points). (c) and (d) show the fit of the experimental data to eqn (4) and (5) at T = 333 K, respectively (see the text for details). The inset in (d) shows the T_{relax} (bars) in the curves of $a(T)$ (red) and $f_{AFM}(T)$ (black).

where a is the cell parameter, a_s is the saturated lattice parameter after the relaxation, f_{AFM} is the AFM phase fraction, $f_{S\text{-}AFM}$ is the saturated f_{AFM} after the relaxation, and t is the time. The relaxation time τ, and the parameter B which considers that in t = 0 s the measurement starts inside the area of phase transition, are parameters of the fitting.

The estimated relaxation time for the structural and magnetic transformation was $\tau_a = (50 \pm 6)$ s and $\tau_f = (50 \pm 5)$ s, respectively. Both parameters relax around the same time, within the estimated error, supporting the idea that a synchronized evolution exists across the magnetoelastic phase transition.

Summary and concluding remarks

Today, the ultimate origin of the first-order magneto-structural transition in FeRh alloys around equiatomic composition is still debated. The question about which transition pushes the other – the magnetic (from a low-temperature AFM to high-temperature FM states) or the structural one (a change of almost 1% in the unit cell volume) – resembles the typical chicken-or-egg interrogation. Moreover, it is well-known that low-volume favors AFM coupling between Fe atoms and an increase of the unit cell volume results in a positive exchange interaction giving rise to FM order. Combining neutron thermo- and time-resolved-diffraction experiments in a bulk $Fe_{49}Rh_{51}$ alloy, we found clear evidence of a kinetic arrest of the AFM phase as well as coexistence of both AFM and FM phases well-above ($\approx$70 K) the temperature at which the first order magneto-structural transition takes place on heating. The latter suggests that the volume expansion is not homogeneous all over the material as the temperature rises. Although most regions increase drastically their volume, exhibiting FM coupling, some other regions remain with a lower volume favoring the AFM state. On increasing the temperature, the cell volume of these AFM regions progressively expands stabilizing the FM state. On cooling down from high temperature (well above the transition, only FM phase is present) we observed that the AFM phase starts to grow around 70 K above the transition, and the whole material becomes AFM just after the transition temperature. However, the FM phase does not follow the same behavior; there is no kinetic arrest below the transition temperature.

In conclusion, the careful analysis of neutron diffraction patterns collected in a wide temperature region including the first order magnetostructural transition of the $Fe_{49}Rh_{51}$ bulk alloy evidences the strong interplay between the lattice and magnetic degrees of freedom of the system, exhibiting a synchronized transformation throughout the phase transition, even under non-equilibrium conditions. Perhaps, the existence of regions with slightly smaller cell volumes in which the AFM sate is more stable gives rise to the asymmetry of the kinetic arrest, only exhibited by the AFM phase.

Author contributions

K. P.-A. & J. L. S. L: conceptualization, investigation, data curation, methodology and formal analysis, writing original draft; G. J. C. & I. P. O: data curation, and formal analysis; J. L.-G: data analysis, validation; M. L. A. H: investigation and data curation; P. G. & P. A.-A: conceptualization, supervision, and funding acquisition. All the authors participated in the writing of the final version.

Data availability

The neutron diffraction data can be found in: **https://doi.org/10.5291/ILL-DATA.5-31-2945**, **https://doi.org/10.5291/ILL-DATA.5-25-290**, **https://doi.org/10.5291/ILL-DATA.CRG-3054**.

Conflicts of interest

There are no conflicts to declare.

Acknowledgements

This work has been partially supported by the following projects: (a) PTDC/EMETED/3099/2020, UIDP/04968/2020-Programatico; (b) PID2022-138256NB-C21, from Spanish MCIN/AEI/10.13039/501100011033 and ERDF, UE; (c) CF-2023-I-2143 from CONAHCYT, Mexico; and (d) SEK-25-GRU-GIC-24-113 from SEKUENS Agency of the Principality of Asturias. K. Padrón-Alemán acknowledges the Institute Laue-Langevin for his PhD/CFR contract (Reference: ESP-5-2023). M.L. Arreguín-Hernandez thanks DGAPA-UNAM and CONAHCYT for supporting her postdoctoral position at UNAM and PhD studies at IPICyT (scholarship 861515; 2023–2020). The authors acknowledge Institute Laue-Langevin for the beam-time allocations 5-31-2945 and 5-25-290 and the Spanish Initiatives on Neutron Scattering (SPINS) for the beam-time allocation CRG-3054.

Notes and references

1 L. H. Lewis, C. H. Marrows and S. Langridge, *J. Phys. D: Appl. Phys.*, 2016, **49**, 323002.
2 A. Zakharov, *Fiz. Met. Metalloved.*, 1967, **24**, 84.
3 R. R. Gimaev, A. A. Vaulin, A. F. Gubkin and V. I. Zverev, *Phys. Met. Metallogr.*, 2020, **121**, 823.
4 C. F. Sánchez-Valdés, R. R. Gimaev, M. López-Cruz, J. L. Sánchez Llamazares, V. I. Zverev, A. M. Tishin, A. M. G. Carvalho, D. J. M. Aguiar, Y. Mudryk and V. K. Pecharsky, *J. Magn. Magn. Mater.*, 2020, **498**, 166130.
5 A. Chirkova, F. Bittner, K. Nenkov, N. V. Baranov, L. Schultz, K. Nielsch and T. G. Woodcock, *Acta Mater.*, 2017, **131**, 31.
6 K. Padrón-Alemán, M. Rivas, J. C. Martínez-García, P. Álvarez-Alonso, P. Gorria, J. H. Belo, A. M. Dos Santos and J. L. Sanchez Llamazares, *J. Alloys Compd.*, 2025, **1010**, 177876.
7 M. L. Arreguín-Hernández, C. F. Sánchez-Valdés, J. L. Sanchez Llamazares, D. Ríos-Jara, V. K. Pecharsky, M. I. Blinov, V. N. Prudnikov, B. B. Kovalev, V. I. Zverev and A. M. Tishin, *J. Alloys Compd.*, 2021, **871**, 159586.
8 M. P. Annaorazov, S. A. Nikitin, A. L. Tyurin, K. A. Asatryan and A. K. Dovletov, *J. Appl. Phys.*, 1996, **79**, 1689.
9 M. P. Annaorazov, K. A. Asatryan, G. Myalikgulyev, S. A. Nikitin, A. M. Tishin and A. L. Tyurin, *Cryogenics*, 1992, **32**, 867.
10 A. Chirkova, K. P. Skokov, L. Schultz, N. V. Baranov, O. Gutfleisch and T. G. Woodcock, *Acta Mater.*, 2016, **106**, 15.
11 H. B. Tran, T. Fukushima, H. Momida, K. Sato, Y. Makino and T. Oguchi, *J. Alloys Compd.*, 2022, **926**, 166718.
12 S. A. Nikitin, G. Myalikgulyev, A. M. Tishin, M. P. Annaorazov, K. A. Asatryan and A. L. Tyurin, *Phys. Lett. A*, 1990, **148**, 363.
13 S. A. Nikitin, G. Myalikgulyev, M. P. Annaorazov, A. L. Tyurin, R. W. Myndyev and S. A. Akopyan, *Phys. Lett. A*, 1992, **171**, 234.
14 A. Gràcia-Condal, E. Stern-Taulats, A. Planes and L. Mañosa, *Phys. Rev. Mater.*, 2018, **2**, 084413.
15 E. Stern-Taulats, A. Planes, P. Lloveras, M. Barrio, J. L. Tamarit, S. Pramanick, S. Majumdar, C. Frontera and L. Mañosa, *Phys. Rev. B*, 2014, **89**, 214105.
16 L. I. Vinokurova, A. V. Vlasov, N. I. Kulikov and M. Pardavi-Horváth, *J. Magn. Magn. Mater.*, 1981, **25**, 201.
17 M. R. Ibarra and P. A. Algarabel, *Phys. Rev. B*, 1994, **50**, 4196.
18 A. Aubert, K. Skokov, G. Gomez, A. Chirkova, I. Radulov, F. Wilhelm, A. Rogalev, H. Wende, O. Gutfleisch and K. Ollefz, *IEEE IEEE Trans. Instrum. Meas.*, 2022, **71**, 1.
19 D. J. Keavney, Y. Choi, M. V. Holt, V. Uhlíř, D. Arena, E. E. Fullerton, P. J. Ryan and J. W. Kim, *Sci. Rep.*, 2018, **8**, 1778.
20 G. Li, R. Medapalli, J. H. Mentink, R. V. Mikhaylovskiy, T. G. H. Blank, S. K. K. Patel, A. K. Zvezdin, T. Rasing, E. E. Fullerton and A. V. Kimel, *Nat. Commun.*, 2022, **13**, 2998.
21 J.-U. Thiele, S. Maat, J. L. Robertson and E. E. Fullerton, *IEEE Trans. Magn.*, 2004, **40**, 2537.
22 G. Shirane, C. W. Chen, P. A. Flinn and R. Nathans, *Phys. Rev.*, 1963, **131**, 183.
23 G. Shirane, C. W. Chen, P. A. Flinn and R. Nathans, *J. Appl. Phys.*, 1963, **34**, 1044.
24 F. Bertaut, F. de Bergevin and G. Roult, *Compd. Rend.*, 1963, **256**, 1668.
25 G. Shirane, R. Nathans and C. W. Chen, *Phys. Rev.*, 1964, **134**, A1547.
26 M. Wolloch, M. E. Gruner, W. Keune, P. Mohn, J. Redinger, F. Hofer, D. Suess, R. Podloucky, J. Landers, S. Salamon, F. Scheibel, D. Spoddig, R. Witte, B. Roldan Cuenya, O. Gutfleisch, M. Y. Hu, J. Zhao, T. Toellner, E. E. Alp, M. Siewert, P. Entel, R. Pentcheva and H. Wende, *Phys. Rev. B*, 2016, **94**, 174435.
27 V. L. Moruzzi and P. M. Marcus, *Phys. Rev. B: Condens. Matter Mater. Phys.*, 1992, **46**, 2864.
28 S. Polesya, S. Mankovsky, D. Ködderitzsch, J. Minár and H. Ebert, *Phys. Rev. B*, 2016, **93**, 024423.
29 N. Kunitomi, M. Kohgi and Y. Nakai, *Phys. Lett. A*, 1971, **37**, 333.
30 E. F. Bertaut, A. Delapalme, F. Forrat, G. Roult, F. De Bergevin and R. Pauthenet, *J. Appl. Phys.*, 1962, **33**, 1123.
31 M. E. Gruner, E. Hoffmann and P. Entel, *Phys. Rev. B: Condens. Matter Mater. Phys.*, 2003, **67**, 064415.
32 V. I. Zverev, R. R. Gimaev, T. Miyanaga, A. A. Vaulin, A. F. Gubkin, B. B. Kovalev, A. M. Dos Santos, E. Lovell,

L. F. Cohen and N. A. Zarkevich, *J. Magn. Magn. Mater.*, 2021, **522**, 167560.

33 L. M. F. de Bergevin, *Bull. Am. Phys. Soc.*, 1962, **6**, 159.

34 C. Stamm, J. U. Thiele, T. Kachel, I. Radu, P. Ramm, M. Kosuth, J. Minár, H. Ebert, H. A. Dürr, W. Eberhardt and C. H. Back, *Phys. Rev. B: Condens. Matter Mater. Phys.*, 2008, **77**, 184401.

35 J. S. Kouvel and C. C. Hartelius, *J. Appl. Phys.*, 1962, **33**, 1343.

36 L. J. Swartzendruber, *Bull. Alloy Phase Diagrams*, 1984, **5**, 456.

37 A. Biswas, S. Gupta, D. Clifford, Y. Mudryk, R. Hadimani, R. Barua and V. K. Pecharsky, *J. Alloys Compd.*, 2022, **921**, 165993.

38 J.-U. Thiele, M. Buess and C. H. Back, *Appl. Phys. Lett.*, 2004, **85**, 2857.

39 G. Ju, J. Hohlfeld, B. Bergman, R. J. M. Van De Veerdonk, O. N. Mryasov, J. Y. Kim, X. Wu, D. Weller and B. Koopmans, *Phys. Rev. Lett.*, 2004, **93**, 197403.

40 S. O. Mariager, F. Pressacco, G. Ingold, A. Caviezel, E. Möhr-Vorobeva, P. Beaud, S. L. Johnson, C. J. Milne, E. Mancini, S. Moyerman, E. E. Fullerton, R. Feidenhans'l, C. H. Back and C. Quitmann, *Phys. Rev. Lett.*, 2012, **108**, 087201.

41 J. Rodriguez-Carvajal, Abstr. Satell. Meet. Powder Diffr. XV Congr. IUCr, 1990, **127**.

42 J. Rodríguez-Carvajal, *Phys. Rev. B: Condens. Matter Mater. Phys.*, 1993, **192**, 55.

43 H. M. Rietveld, *J. Appl. Crystallogr.*, 1969, **2**, 65.

44 B. D. Cullity and C. D. Graham, *Introduction to Magnetic Materials*, 1st edn Wiley, 2008.

45 C. R. Pike, A. P. Roberts and K. L. Verosub, *J. Appl. Phys.*, 1999, **85**, 6660.

46 V. Franco, T. Gottschall, K. P. Skokov and O. Gutfleisch, *IEEE Magn. Lett.*, 2016, **7**, 1.

47 L. M. Moreno-Ramírez and V. Franco, *Metals*, 2020, **10**, 1039.

48 Á. Díaz-García, L. M. Moreno-Ramírez, J. Y. Law, F. Albertini, S. Fabbrici and V. Franco, *J. Alloys Compd.*, 2021, **867**, 159184.

49 A. Aubert, K. Skokov, A. Rogalev, A. Chirkova, B. Beckmann, F. Maccari, E. Dilmieva, F. Wilhelm, V. Nassif, L. V. B. Diop, E. Bruder, J. Löfstrand, D. Primetzhofer, M. Sahlberg, E. Adabifiroozjaei, L. Molina-Luna, G. Gomez, B. Eggert, K. Ollefs, H. Wende and O. Gutfleisch, *ACS Appl. Mater. Interfaces*, 2024, **16**, 62358.

50 A. S. Komlev, D. Y. Karpenkov, D. A. Kiselev, T. S. Ilina, A. Chirkova, R. R. Gimaev, T. Usami, T. Taniyama, V. I. Zverev and N. S. Perov, *J. Alloys Compd.*, 2021, **874**, 159924.

51 E. C. Stoner and E. P. Wohlfarth, *IEEE Trans. Magn.*, 1991, **27**, 3475.